

**A high-resolution OGCM simulation of the Tropical Pacific Ocean during
the 198 S-1994 TOGA period. Part 1: Long equatorial waves.**

J.-P. Boulanger*, F. Delecluse, C. Maes and C. Lévy

Laboratoire d'Océanographie Dynamique et de Climatologie

Unité mixte de recherche CNRS/ORSTOM/UPMC

4, Place Jussieu 75252 Paris Cedex 05

* Presently at:

Jet Propulsion Laboratory
4800 Oak Grove Drive
Pasadena CA 91109, USA

Journal of Climate

June 1995

Submitted to Month] y Weather Review (TOGA Special Issue)

Abstract

A high resolution oceanic general circulation model of the three tropical oceans is used to investigate long equatorial wave activity in the Pacific ocean during the 1985-1994 TOGA period. Zonal wind stress forcing and simulated dynamic height are interpreted using techniques previously applied to data, Kelvin and first Rossby waves are observed propagating during all the period. A seasonal cycle and interannual anomalies are computed for each long equatorial wave. The east Pacific basin is mainly dominated by seasonal cycle variations while strong interannual anomalies are observed west of the dateline. Long wave interannual anomalies are then compared to wave coefficients simulated by a simple wind-forced model. Our results outline the major role played by wind forcing on interannual time scales in generating long equatorial waves. However, near both eastern and western boundaries, some differences can be attributed to long wave reflections. A comparison to wave coefficients calculated from GEOSAT sea-level data gives some insight of the model behavior.

I. Introduction

A major success of the 1985-1994 TOGA (Tropical Ocean-Global Atmosphere) program is "the continuation and/or development of ocean observing systems such as Volunteer Observing System, Tropical Atmosphere Ocean (TAO) buoy array, Surface Velocity Program,... During the TOGA decade, satellites (GEOSAT and TOPEX/POSEIDON altimeters) provided large scale sea-level measurements over two El Nino and one La Nina events. Both satellite data and *in-situ* data from the TOGA-TAO buoy array contributed to a large coverage and high-accuracy observations of the tropical Pacific ocean (McPhaden, 1993; Menkes et al., 1995), and allow now to investigate theoretical mechanisms hypothesized for El Nino/Southern Oscillation (ENSO) variability (Delcroix *et al.*, 1994, hereafter D94; Kessler and McPhaden, 1995; Boulanger and Menkes, 1995, hereafter BM).

Various theories, such as a warm water buildup in the western Pacific ocean (Wyrtki, 1975), the delayed action oscillator mechanism (Schopf and Suarez, 1988) or the SST mode in the fast wave limit (Neelin, 1991), have been suggested to play a role in ENSO variability. Considering more particularly the delayed action oscillator theory, its mechanism involves the linear ocean dynamics through propagation and reflection of long equatorial waves (Battisti, 1988). Mainly, the Kelvin and three gravest Rossby waves are expected to play an important role in equatorial ocean dynamics and ENSO variability. Kelvin waves were first observed through meridional shape of their sea-level signature (Rips and Hayes, 1981) and in eastward propagating signal (Knox and Halpern, 1982). First meridional Rossby waves were evidenced in *in situ* data by Lukas *et al.* (1984) and Lukas and Firing (1985). Using altimetric GEOSAT data, Mille *et al.* (1988) and, later, Delcroix *et al.* (1991) demonstrated nice propagations of these waves throughout most of the basin. Also using observations from the GEOSAT altimeter covering the 1986-1987 El Nino and 1988-1989 La Nina events, D94 evidenced Kelvin and first Rossby wave propagations over most of the Pacific ocean, described their variability with ENSO conditions and evaluated their contributions to sea-level and geostrophic zonal current

anomalies. But only with TOPEX/POSEIDON altimeter accuracy, second and third Rossby waves were observed propagating at theoretical speeds (BM). Thus, while linear ocean dynamics and long equatorial waves have been first viewed as a useful, and demonstrated powerful, approach for the understanding of the oceanic low-frequency variability, they are now quantitatively used to interpret sea-level and zonal geostrophic current anomalies and, most of all, sea surface temperature variability (Picaut and Delcroix, 1995).

However, many questions about the role played by long waves still remain. Recent works interpreted sea-level and dynamic height variability in terms of long equatorial waves of the first baroclinic mode, thus it is important to determine to what extent the sea surface variability in the tropical Pacific ocean can be explained by linear long equatorial waves. In particular, reflections at both eastern and western boundaries, high Rossby mode contributions and ageostrophic processes must be examined. Moreover, as derived geostrophic zonal currents are used to calculate sea surface temperature zonal advection, the variance of zonal currents explained by geostrophic adjustment must be estimated, and the actual contribution of long equatorial waves to sea surface temperature zonal advection then quantified. The latter point will be examined in a forthcoming paper (Boulanger *et al.*, 1995). Unfortunately, the former question cannot be assessed by comparing wind forcing and sea-level variability over the whole tropical Pacific ocean on long time scales as we lack a large scale and space/time high density observing system. Thus, we decided to force a high-resolution oceanic general circulation model and a simple wave model by the same wind forcing, and to compare their responses in terms of long equatorial waves. This approach allows us to identify the role played by the wind forcing, to quantify long wave reflections and to assess to what extent long equatorial waves of a single baroclinic mode can explain sea-level variability.

The oceanic general circulation model (OGCM) we used was adapted to the tropical Pacific ocean and tested in different experiments. The early runs were developed and extensively detailed by Dandin (1993). The model participated to a TOGA-NEG

(Numerical Experiment Group) intercomparison (Stockdale *et al.*, 1993) which specified the typical biases of models forced by climatological conditions. The present version of the model slightly differs from the above version (mainly in spatial coverage and topography). However, the physical parameters have similar values. The velocity fields from the run discussed here were compared to the mean seasonal drifter fields from the Surface Velocity Programme (Niiler *et al.*, 1995) and present variances in both zonal and meridional velocity components similar to observations.

In this first paper, we are interested in evaluating the role played by long equatorial waves in a high-resolution tropical OGCM simulation. First, we interpret the simulated dynamic height in terms of long, equatorial waves in a way similar to other works on observations (D94; BM). Our aim is to determine whether long equatorial waves can be identified in an OGCM simulation and whether they play a role similar to the one observed in the real ocean. Recent studies have interpreted both sea-level and zonal geostrophic current anomalies, as well as temperature variations, in relation to long equatorial wave activity. Therefore, we compare the OGCM simulation to a simple wind-forced wave-model, and we estimate to what extent a single vertical baroclinic mode of the linear ocean dynamics can explain the simulated dynamic height variability.

The arrangement of this paper is as follows. In section 2, the model is detailed. In section 3, we describe the simulated fields, briefly present the method used for the calculation of long equatorial wave coefficients and estimate the variance of dynamic height and zonal wind stress explained by Kelvin and first Rossby modes in the equatorial band. In section 4, these coefficients, as well as their seasonal cycle, are described. In section 5, the wave forcing coefficients are integrated along wave characteristics, and interannual anomalies are compared to previously calculated wave coefficients. In section 6, we compare qualitatively Kelvin and first Rossby wave coefficients to those calculated from GEOSAT sea-level data. Finally, in section 7, we conclude about the individual propagation of long equatorial waves in our simulation of

the TOGA period, and we introduce some questions which are investigated in a forthcoming paper.

II. Model

This study was performed with the OGCM developed at the LODYC (OPA version 7, Delecluse *et al.*, 1993). It solves the primitive equation (i.e. Navier-Stokes equations plus some classical additional assumptions: Boussinesq and hydrostatic approximations, incompressibility), assuming the sea surface to be a rigid lid boundary. The *in-situ* density is computed following the formulation given in Millero and Poisson (1981). These equations are written in tensorial formalism so that they are suited to any three dimensional orthogonal curvilinear mesh on the sphere. The use of vectorial operators ensures a second order accuracy on the grid (Marti *et al.*, 1991). The equations are discretized in finite differences on a staggered “C” grid (Arakawa, 1972) and the finite difference equations can be found in Delecluse *et al.* (1993). The time stepping is achieved with a basic leapfrog differencing structure associated with a Asselin (1972) time filter while a forward scheme is used for the turbulent horizontal diffusion terms and an implicit scheme for the turbulent vertical diffusion terms. The time step is set to one hour. No-slip boundary conditions and no flux conditions for heat and salt are applied at the bottom and along the coastlines, while the surface fluxes of momentum, salinity and heat are prescribed through the specification of the wind-stress, the fresh water budget, the penetrative solar flux and the net heat budget at the sea surface.

The sub-grid physics is parametrized as follows : 1/- Vertical mixing coefficients are computed from a 1.5 turbulent closure model in which the turbulent kinetic energy (TKE) is computed through a prognostic equation while the turbulent length scales are defined by a diagnostic formulation. This parameterization has been embedded in the LODYC OGCM by Blanke and Delecluse (1993) for tropical simulations. The delicate point of the closure assumption lies in the formulation of the turbulent length scale which

is defined as the length scale required to convert the $TKI\dot{E}$ into potential energy. 2/- Lateral mixing is explicit by a second order operator and the value of the horizontal viscosity and diffusivity are positive constants equal to $103 \text{ m}^2/\text{s}$. These magnitudes are taken following the sensitivity experiments presented by Mac *et al.* (1995). This study shows that a large value of these coefficients (an order larger) can modify the large scale response of the model as a low value (an order smaller) leads to an enhanced response of the vertical physics. The medium value is kept herein the equatorial region until 20°N and 20°S , and smoothly increases till the lateral boundaries.

The model domain covers the three tropical oceans between 50°N and 50°S . The mesh has a classical geographical configuration (latitude-longitude) and the third axis is the local vertical. The zonal mesh is determined by analytical functions where the resolution is increased each time that a coastline crosses the equator. The zonal resolution is equal to 0.33° and rises until 0.75° in the middle of oceanic basins. The meridian resolution is also irregular with smallest value of 0.33° at the equator, increases to 1.5° at the northern and southern boundaries. The vertical mesh is defined through 30 levels until a 5000 m threshold. The minimum resolution is set to 10 meters in the 16 upper levels and increases after the level 24 (deeper than 600 m). The bottom topography field is derived from the $5'\times 5'$ ETOPO5 data set (Marine Geology and Geophysics Division, National Geophysical Data Center, Boulder, Colorado) averaged over each model grid box. The model presents a connection between the Indian and the Pacific oceans which is investigated in Mats and Delecluse (1995).

The experimental forcing conditions (wind stress, heat fluxes and fresh budget) are taken from the climate version of ARPEGE whose main characteristics are presented by Déqué *et al.* (1994). The atmosphere model has been run during the TOGA period (1985-1994) using the observed SST (Reynolds and Smith, 1994) as a lower boundary condition. The forcing fields used in this study are extracted daily from the T42 spectral model. The surface heat flux is then parameterized as follows :

$$Q = Q_{\text{Arpege}} + dQ/dT * (SST - SST_{\text{ob}})$$

where $Q_{Arpegge}$ is given by the atmosphere model, SST_{ob} is the observed sea surface temperature of Reynolds and Smith (1994), and SST is the first level temperature of the model. The negative feedback term dQ/dT is set to $-40 \text{ W/m}^2/\text{K}$, a typical value over the equatorial Pacific ocean (Oberhuber, 1988). The solar flux is allowed to penetrate below the top model layer; its attenuation with depth follows the formulation of Paulson and Simpson (1977) with a Jerlov (1968) optical water type I. About one half of the solar flux is absorbed into the first top decimeters while the remaining part is absorbed within the few ten meters,

During the computation, a linear restoring term towards the monthly mean temperature and seasonal salinity fields of Levitus (1982) is only applied poleward of 20°N/S and under the mixed-layer. The restoring coefficient value varies in function of depth and latitude (it increases poleward from $(250 \text{ days})^{-1}$ at 20°N/S to $(30 \text{ days})^{-1}$ at boundary). The model starts in January, with Levitus' salinity and temperature, and was spun up from rest (by repeating twice the 1984 year).

III. Zonal wind stress and dynamic height fields

We are interested in studying a simulation of the Pacific ocean in a way similar to recent works on observed sea-level, dynamic height or geostrophic zonal current anomalies (e.g. D94; BM; Kessler and McPhaden, 1995). Therefore, our study focuses on low-frequency surface dynamic height (relative to 1000dbar) and zonal wind stress anomalies. Both fields have a 5-day time step, and are filtered in time with a 55-day Hanning filter.

Zonal wind stress and dynamic height decompositions. The decomposition methods used to project zonal wind stress anomalies and dynamic height anomalies onto long equatorial waves are described in BM. A similar procedure was followed to validate the methods near the boundaries, and identical results were found. We briefly remind the major steps. First, using simulated dynamic height anomalies, a time-lag' correlation

analysis was performed at the equator and at 4°N. A mean baroclinic phase speed of 2.5m/s was estimated (this result will be detailed later). We kept this value to calculate a Rossby radius (332km) and, then, calculate long equatorial wave structures (Fig. 1). Dynamic height anomalies were then assumed to be written as a sum of these long equatorial waves and decomposed onto these waves following BM's method (see their appendix A3). Zonal wind stress anomalies were identically decomposed onto long equatorial wave structures following BM's method (see their appendix A4).

Preliminary results. For each coefficient (Kelvin and first Rossby), a time-lag correlation analysis (Delcroix *et al.*, 1991) is used to calculate a mean phase speed and estimate an error on this value. Results are respectively for both wave coefficients $2.20 \pm 0.5 \text{ m/s}$ and $-0.80 \pm 0.5 \text{ m/s}$. They are thus consistent with our first estimate of 2.50m/s.

Then, a zonal wind stress field and a dynamic height field are reconstructed considering only Kelvin and first Rossby signals. These reconstructed fields are then compared to the original fields.

a) Zonal wind stress. Correlation (Fig. 2b) and explained variance (Fig. 2c) are very high along the equator, but both decrease rapidly poleward of 2°N/S. Thus, forcing reconstructed from the Kelvin and first gravest Rossby modes does not explain the entire high-value pattern observed between 140°W and 110°W (Fig. 2a), neither off-equatorial maxima observed in the western Pacific in both hemispheres. As we will see later, the east Pacific maximum can be attributed to the seasonal cycle, while near dateline high values are mainly related to the interannual signal.

b) Dynamic height. Correlation (Fig. 3b) and explained variance (Fig. 3c) between original and reconstructed dynamic height anomaly fields are respectively higher than 0.9 and 90% throughout the Pacific ocean in a 3°N/3°S band. Hence., all the equatorial variability observed on Fig. 3a (near the dateline and in the east Pacific, both in relation with local maxima observed in the wind pattern) is fairly well explained. However, both

off-equatorial maxima in the northern hemisphere (one in the western Pacific, the other between 5°N and 8°N in the east Pacific) cannot be represented by the two long equatorial waves we are considering in this study.

Having these above limitations in mind, we will now pursue the study and discuss the long wave signals.

IV. Long wave coefficients

Seasonal cycle versus interannual anomalies. Long equatorial wave coefficients are anomalies relative to the mean calculated over the 1985-1994 period. A seasonal cycle is computed for each coefficient averaging years 1985 to 1994. Interannual anomalies are relative to this seasonal cycle. We computed standard deviations of the coefficients, of their seasonal cycle and of their interannual anomalies. Results are displayed on Figure 4a-b. A first look at the two equatorial wave coefficients shows that the basin is mostly split into two halves. In the western half of the basin (west of the dateline), interannual anomalies are predominant while, in the eastern half, the seasonal cycle is the strongest signal. The strong variability observed on Figure 2a between 140°W and 110°W is mainly due to zonal wind stress seasonal signal. On its east side, Kelvin waves are generated, and we can observe on Figure 4a a strong seasonal component east of 110°W. On its west side, first Rossby waves are generated, a strong seasonal signal is seen on Figure 4b from 140°W to the dateline. The other important seasonal contribution near the eastern boundary (Fig. 4b) may come from the reflection of Kelvin waves. This point will be examined later. We will show in the following that the strong seasonal cycle contribution east of the dateline can be explained as a local response to zonal wind stress seasonal Cycle.

Kelvin and first Rossby mode coefficients are displayed on Fig. 5a-b. Confirming previous results, two distinct regimes are observed in the basin. East of 140°W , the wave signal is largely dominated by the seasonal cycle (Fig. 6a-b). This feature is coherent with the wind annual cycle (Fig. 7a-b). The Trades weaken in Spring as the ITCZ is moving equatorward, and SST warms up. Annual westerly anomalies are thus observed in the central-east Pacific and generate downwelling Kelvin and upwelling first Rossby waves. Both contribute to the seasonal warming of the eastern Pacific ocean as follows: both waves induce eastward current anomalies, and contribute to advect warmer waters from the west, while the Kelvin wave deepens the thermocline in the east (therefore decreases the cooling effect of upwelling on SST). It is worth noting that the annual upwelling first Rossby wave (Fig. 6b) is not coming from the eastern boundary but is wind-forced near 110°W (Fig. 7b). Then, during Summer and Fall, the Trades reinforce inducing annual easterly anomalies which force upwelling Kelvin and downwelling first Rossby waves. These waves will act in an opposite way to previously described waves. Although annual positive first Rossby wind forcing in Fall is located between 160°W and 90°W (Fig. 7b), as the annual negative forcing in Spring, the downwelling first Rossby wave is observed propagating from the eastern boundary in late Spring, at a time the annual downwelling Kelvin wave is reaching the boundary. Therefore, the downwelling first Rossby wave seems to be first generated by reflection of the downwelling Kelvin wave and lately forced along its path by local winds.

Now focusing our attention on the western half of the basin, the variability seems there to be mainly influenced by interannual variability. Indeed, the Kelvin seasonal cycle in the west Pacific ocean has not much amplitude (Fig. 6a). Its dominant feature is a downwelling signal generated in early Winter by westerly anomalies located between 160°E and 180 . This wave propagates to the eastern Pacific that it reaches in beginning of January. The first Rossby wave annual signal in the western Pacific (Fig. 6b) is characterised in Fall by the arrival of the annual upwelling wave and in Spring of a

downwelling wave wind-forced west of the dateline. however, the first Rossby wave annual signal has not much amplitude in the western Pacific compared to the total signal (Fig 4b). Indeed, strong interannual signals are observed in relation with simulated ENSO variability. Considering first the warm El Nino events, the 1986-1987, 1991-1992 and 1992-1993 warmings are terminated by the propagation of strong upwelling first Rossby waves from the central to the western Pacific. This wave always appears as a strengthening of the annual upwelling wave. However, while strong upwelling waves (Kelvin and first Rossby) are seen on Figures 5a-bin tile central and east Pacific during the 1988-1989 La Nina event, no strong downwelling first Rossby wave is observed propagating throughout the basin at its end. A further discussion on interannual signal is presented in the following section.

V. Interannual variability and wind-forced contribution

To estimate how wind-forcing is responsible of wave generation, we developed a simple wind-forced wave model. For each wave, forcing coefficients are integrated along wave characteristics from 130°E to 80°W for the Kelvin mode and from 80°W to 130°E for the first Rossby mode. For each wave, the model integrates the following equation:

$$(\partial_t + c_n \partial_x + r_n) a_n = F_n(x, t) / D$$

where phase speeds of wave propagation (c_n) are assumed to be 2.5m/s and -0.83m/s, r_n is a damping time taken to be (3 months)] for Kelvin and first Rossby modes, F_n are the forcing coefficients, D is a wind-projection depth and a_n are the coefficients to be calculated, No reflection at the boundaries is taken into account, thus only wind forcing contribution is shown. A discussion on the parameter choice is beyond the scope of this paper, but it will be done in a subsequent paper. However, our choice is coherent with estimates made by Picaut *et al.* (1993) and Kessler and McPhaden (1995) comparing simple models and data. D was estimated by comparing standard deviations of projected coefficients (see part 4) and integrated coefficients. Its value is taken to be 100m. In the

following, only comparisons between interannual anomalies of calculated wave coefficients from the simulated dynamic height anomalies (called 01'A coefficients) and of integrated wave coefficients from the simple wind-forced model (called SIMO coefficients, SIMO for Simple MOdel) are discussed.

Comparison between Figures 8a and 8b clearly shows that most of the Kelvin type variability observed in central and east Pacific. is fairly well explained in terms of wind forcing. Indeed, either amplitude and phase are well reproduced by the simple wind-forced model]. However, major differences are observed in the western Pacific where reflections may potentially play an important role. For the Rossby wave component (Figs. 9a and 9b), variability in central and western Pacific is also fairly well explained by the simple model. But major differences are observed in the eastern Pacific, where signals reflected from incoming Kelvin waves may have a large contribution. We now describe interannual anomalies in light of the simple model results.

First, preceding both 1986-1987 and 1991-1992 El Nino events,, Kelvin wave signal in the western Pacific lacks strong downwelling amplitude (Fig.8b). From early 1985 to November 1986, downwelling Kelvin signal is located from 130°E to the dateline (Fig. 8a). This coherent signal over almost two years seem to. be attributed to first Rossby wave reflections at the western boundary. indeed, strong downwelling first Rossby waves are forced near the dateline over this period (Figs. 9a and 9b). During the same period, upwelling Kelvin waves are generated to the east (Fig.8b). This signal is not clearly observed on Figure 8a as downwelling Kelvin waves coming from western boundary reflection are superimposed to the negative amplitudes and nearly cancel them. A similar scenario is at work from the end of 1988 to the end of 1990. Strong downwelling first Rossby waves are wind-forced near the dateline and seem to reflect into downwelling Kelvin waves. Still considering Kelvin signal, other differences between Figures 8a and 8b are observed from the end of 1987 and during the 1991-1993 period. On July 1987, a strong westerly anomaly located near the dateline generated a downwelling Kelvin wave and an upwelling first Rossby wave. The latter reached the

western boundary, on the end of 1987 simultaneously, to the generation of an upwelling Kelvin signal in this region. During the 1991-1993 period, upwelling first Rossby waves are wind-forced near the dateline and seem to be responsible of the upwelling Kelvin signals observed on Figure 8a and not present on Figure 8b. These differences between OPA and SIMO Kelvin coefficients indicate that western boundary reflections exist and play a role in the low-frequency variability of our oceanic general circulation model simulation.

Now focusing our attention on Figures 9a and 9b, it is obvious that the downwelling Rossby signal observed in the west Pacific previously to the 1986-1987 and 1991-1993 El Nino events is indeed wind-forced. Major differences are observed during the 1986-1989 period. On the beginning of 1987 and during the second half of this year strong downwelling first Rossby signals are observed coming from the eastern boundary. Although partially wind-forced, they are in phase with a potential reflection of strong downwelling Kelvin waves forced in late 1986 and in July 1987. Later during the 1988-1989 La Nina event, the strong upwelling Rossby wave signal is not observed on Figure 9b but is coherent with the arrival of strong upwelling Kelvin waves on the eastern boundary. Other differences between Figures 9a and 9b seem to be attributed to Kelvin wave reflections on the eastern boundary. Eventually, the downwelling signal in 1988-1989 in the western Pacific is much stronger in SIMO than in OPA coefficients. This difference may come from the lack of upwelling Rossby waves coming from the reflection and propagating to the western Pacific.

Hence, the described discrepancies between OPA and SIMO wave coefficients over the TOGA period clearly show that, in this model, Kelvin wave reflection at the eastern boundary and first Rossby wave reflection at the western boundary may play a role in the central Pacific interannual variability. To estimate if such a behavior is realistic, a comparison to Kelvin and first Rossby wave coefficients calculated from GEOSAT sea-level data is now examined.

VI. Comparison to GEOSAT long wave coefficients

GEOSAT sea-level data were presented in Delcroix *et al.* (1994). Briefly, sea-level anomalies are relative to the November 1986-October 1988 period, they are gridded on a 5° longitude x 0.5° latitude x 5days, and filtered in longitude with a 15° Hanning filter, in latitude with a 3.5° Hanning filter and in time with a 35-day Hanning filter. Thus, some discrepancies between GEOSAT results and our simulation may come from differences in processing and filtering. Moreover, D94 compared their GEOSAT sea-level data set to *in-situ* data, and they showed that results in the east Pacific were worse than in central and west Pacific. q'bus, the model-data misfits, east of 110°W , will not be discussed.

The sea-level data set was decomposed onto long equatorial waves using the same method than used on the model i.e. the assumed phase speed is taken to be 2.5m/s. This is different from the 2.8m/s choice made by D94. However, as they argued and as can be observed when comparing our results to their Figures 3b-c, choosing different phase speed $\pm 10\%$ does not affect main conclusions on wave propagation. To be compared to GEOSAT results, OPA long wave coefficients are relative to the same period (Nov. 86-Oct. 88). Results are displayed on Figures 10a-d.

As previously shown, most of the simulated Kelvin (resp. first Rossby) wave variability is explained in the central and east Pacific (resp. central and west Pacific) by the Arpege wind-forcing. Thus, amplitude misfits between OPA and GEOSAT wave coefficients can be attributed to Arpege wind biases, and to GEOSAT sea-level signal. The lack of GEOSAT sea-level amplitude is confirmed by D94's table 1. Indeed, they computed GEOSAT sea-level standard deviation at mooring and tide gauge locations and showed that, on a mean, the ratio between GEOSAT and *in-situ* data standard deviation is equal to 0.7. As we showed, in the previous section, most of the OPA wave variability is explained by Arpege wind forcing. Thus, differences in wave variability between OPA and GEOSAT can mainly be attributed to differences between Arpege and "real" winds. Therefore, in the following, we describe model-data agreements and differences qualitatively, and we mainly focus on signals which maybe influenced by reflections.

variability during the TOGA period, describe the role played by wind-forcing and give some indications of potential reflections at both eastern and western boundaries.

The simulation was performed with the OGCM developed at the LODYC (Delecluse *et al.*, 1993) and adapted to the Pacific ocean by Maes *et al.* (1995). Our present version covers the three tropical oceans between 50°N and 50°S. The forcing fields are taken from a simulation of the TOGA period by the climate version of ARPEGE. We focus on zonal wind stress and dynamic height (relative to 1000dbar) fields filtered with a 55-day Hanning filter.

Both zonal wind stress and dynamic height fields are decomposed in terms of long equatorial waves using the method described by Boulanger and Menkes (1995). Kelvin and first Rossby wave propagations are observed at phase speeds typical of a first baroclinic vertical mode (2.5m/s). Zonal wind stress and dynamic height fields are reconstructed considering only Kelvin and first Rossby contributions and are then compared to original fields. While only zonal wind stress variability in a narrow band around the equator (2°N/S) is well reproduced by the reconstructed field, dynamic height variance in 5°N/S is fairly well explained by the two equatorial waves. However, it is worth noting that strong off-equator signals can not be represented. Besides, examination of seasonal signal and interannual anomalies leads to the conclusion that Kelvin and first Rossby wave seasonal signals are dominant east of the dateline while interannual anomalies are stronger west of the dateline.

To describe interannual anomalies and potentially important reflections at both eastern and western boundaries, wave forcing coefficients are integrated along Kelvin and first Rossby wave characteristics assuming a phase speed of 2.5m/s. No reflection at both boundaries is taken into account in this simple wind-forced model. It clearly appears that Kelvin (resp. first Rossby) waves in central and east (resp. central and west) Pacific are, on interannual time scales, mainly wind forced near the dateline. However, major differences between projected and integrated coefficients are observed in west (resp. east) Pacific and seem related to first Rossby (resp. Kelvin) reflections.

To confirm the importance of reflections, we qualitatively compared OPA coefficients to those calculated from GEOSAT sea-level data. The overall features are consistent between both coefficients. However, differences are observed from October 1988 to February 1989 when first Rossby waves are strongly negative from the dateline to 11°W in our simulation but not in GEOSAT data. It seems thus possible that eastern boundary reflections are too important in the model. Western boundary reflections were not examined as our GEOSAT data set has no data west of 150°E .

In conclusion, Kelvin and first Rossby waves are observed propagating individually in the model as in data. Moreover, a single baroclinic mode signal (tuned in amplitude) explains fairly well Kelvin and first Rossby wave variability either in phase and amplitude. However, this study does not fully quantify the role played by long equatorial waves. First, although reflections seem to play an important role in the model, they must be further examined. To assess their contribution to sea-level variability in model and data, we studied both eastern and western boundary reflections in this simulation and in TOPEX/POSEIDON data. Our results will be presented in a subsequent paper. Second, while long equatorial waves explain a large part of sea-level variance in the equatorial band, their role in coupled mechanisms i.e. in sea surface temperature variations (in particular through zonal advection) is not clearly understood. In a second paper, geostrophic zonal currents are studied and the contribution of long equatorial waves examined,

Acknowledgements:

Funding for this study was provided by CNRS (Centre National de la Recherche Scientifique). The atmospheric forcing was provided by the CNRM (Centre National de Recherche de METEOFRANCE). This work was terminated while J.-P. Boulanger was at Jet Propulsion Laboratory, and we want to thank especially Dr Lee I... Fu. Support for computation was provided by the Conseil Scientifique of the IDRIS (Institut du Développement et des Ressources en Informatique Scientifique).

The research described in this publication was carried out by the Jet Propulsion Laboratory, California Institute of Technology, under a contract with the National Aeronautics and Space Administration,

References:

- Arakawa, A., 1972: Design of the UCLA general circulation model. Numerical simulation of weather and climate, Dept. of Meteorology, University of California, **Rep 7**, 1 16pp.
- Asselin, R., 1972: Frequency filter for time integration. *Mon. Wea. Rev.*, **100**, 487-490.
- Battisti D. S., 1988: Dynamics and thermodynamics of a warming event in a coupled tropical atmosphere-ocean model, *J. Atmos. SC.*, **4S**, 2889-2819.
- Blanke, B. and P. Delecluse, 1993: Variability of the tropical Atlantic ocean simulated by a general circulation model with two different mixed-layer physics. *J. Phys. Oceanogr.*, **23**, 1363-1388.
- Bougeault, P. and P. Lacarrère, 1989: Parameterization of orography-induced turbulence in a meso-beta scale model. *Mon. Wea. Rev.*, **117**, 1872-1890.
- Boulanger, J.-P. and C. Menkes, 1995: Propagation and reflection of long equatorial waves in the Pacific ocean during the 1992-1993 El Nino event, submitted to *J. Geophys. Res.*
- Boulanger, J.-P., and P. Delecluse, A high-resolution OGCM simulation of the tropical Pacific ocean during the 1985-1994 TOGA period. Part II: Geostrophic zonal currents, in preparation.
- Dandin, P., 1993: Variability basse fréquence simulée clans le Pacifique tropical, *Thèse de Doctorat de l'Université Paris VI*, 342pp.
- Delecluse, P., G. Madec, M. Imbard and C. Levy, 1993: OPA version 7 ocean general circulation model reference manual. Rapport interne LODYC 93/05, 111 pp.
- Déqué, M., C. Dreveton, A. Braun and D. Cariolle, 1994 : The ARPEGE/IFS atmosphere model: a contribution to the French community climate modeling. *Climate Dynamics*, **10**, 249-266,
- Delcroix, T., J.-P. Boulanger, F. Masia, and C. Menkes, 1994: GEOSAT-derived sea-level and surface-current anomalies in the equatorial Pacific, during the 1986-1989 El Niño and La Niña, *J. Geophys. Res.*, **99**, 25093-25107.
- Delcroix T., J. Picaut, and G. Eldin, 1991: Equatorial Kelvin and Rossby waves evidenced in the Pacific Ocean through GEOSAT sea level and surface current anomalies, *J. Geophys. Res.*, **96** suppl., 3249-3269.
- Gaspar, P., Y. Grégoris and J. M. Lefevre, 1990: A simple eddy-kinetic-energy model for simulations of the oceanic vertical mixing : tests at station Papa and Long-Term Upper ocean Study site. *J. Phys. Oceanogr.*, **95**, 16179-16193.
- Jerlov, N. G., 1968: *Optical Oceanography*. Elsevier Ed., 194 pp.
- Kessler W. S., and M. J. McPhaden, 1995: Equatorial waves and the dynamics of the 1991-1993 El Niño, submitted to.) *Climate*.
- Knox, R. A., and D. Halpern, 1982: Long range Kelvin wave propagation of transport variations in Pacific Ocean equatorial currents, *J. Mar. Res.*, **40**, Suppl., 329-339.
- Kolmogorov, A. N., 1942: The equation of turbulent motion in an incompressible fluid. *Izv. Akad. Nauk. SSSR, Ser. Fiz.*, **6**, 56-58.
- Levitus, S., 1982: Climatological atlas of the world ocean. NOAA Prof. Paper, **13**, NOAA.
- Lukas, R., S. P. Hayes, and K. Wyrtki, 1984: Equatorial sea-level response during the 1982-1983 El Niño, *J. Geophys. Res.*, **89**, 10425-10430.
- Lukas, R., and E. Firing, 1985: The annual Rossby wave in the central equatorial Pacific Ocean, .1. *Phys. Oceanogr.*, **15**, 55-67.
- McPhaden M. J., 1993: TOGA-TAO and the 1991-93 El Niño-Southern Oscillation event, *Oceanography*, **6**, 36-44.
- Madec, G., M. Chartier, P. Delecluse and M. Crépon, 1991: A three dimensional numerical study of deep water formation in the northwestern Mediterranean Sea. *J. Phys. Oceanogr.*, **21**, 1349-1371.
- Mats, C., G. Madec and P. Delecluse, 1995: Sensitivity y of an equatorial Pacific OGCM to the lateral diffusion. *submitted to Monthly Weather Review*,

- Maes, C. and P. Delecluse, 1995: On the throughflow impact on the Indonesian seas and the Pacific ocean. submitted to *JGR*.
- Mar[i, O., G. Madec and P. Delecluse, 1992: Comment on "Net diffusivity in ocean general circulation models with nonuniform grids" by F.L. Yin and I.Y. Fung. *J. Geophys. Res.*, **97**, 12763-12766.
- Menkes, C., J.-P. Boulanger, and A. J. Busalacchi, 1995: Evaluation of TOPEX/POSEIDON sea-level/derived currents and TOGA-TAO dynamic height/derived currents, submitted to *J. Geophys. Res.*
- Miller L., R. Cheney, and B. Douglas, 1988: GEOSAT altimeter observations of Kelvin waves and the 1986-1987 El Niño, *Science*, 239, 52-54.
- Millero, F. S. and A. Poisson, 1981: An international one-atmosphere equation of state of sea water. *Deep Sea Res.*, **28A**, 625-629.
- Neelin, J. D., 1991: The slow sea surface temperature mode and the fast-wave limit: Analytic theory for tropical interannual oscillations and experiments in a hybrid coupled model, *J. Atmos. Sci.*, 48, 584-606.
- Paulson, C. A. and J. J. Simpson, 1977: Irradiance measurements in the upper ocean. *J. Phys. Oceanogr.*, 7, 952-956.
- Picaut, J., and T. Delcroix, 1995: Equatorial wave sequence associated with warm-pool displacements during the 1986-1989 El Niño-La Niña, submitted to *J. Geophys. Res.*
- Picaut, J., C. Menkes, J.-P. Boulanger and Y. du Penhoat, 1993: Dissipation in a Pacific equatorial long wave model, TOGA-Notes, 11-15, 10.
- Reynolds, R. W. and Smith, 1994: Improved global sea surface temperature analyses using optimum interpolation. *J. Climate*, 7, 929-948.
- Ripa, P., and S. Hayes, 1981: Evidence for equatorially trapped waves in the Galapagos Islands, *J. Geophys. Res.*, **86**, 6509-6516.
- Schopf, P. S., and M. J. Suarez, 1988: Vacillations in a coupled ocean-atmosphere model, *J. Atmos. Sci.*, 45, 549-566.
- Stockdale, T., D. Anderson, M. Davey, P. Delecluse, A. Kattenberg, Y. Kitamura, M. Latif and T. Yamagata, 1993: Intercomparison of tropical Pacific ocean GCM'S. WCRP 79, WMO/TD-545.
- Wyrtki K, 1975: El Niño-The dynamic response of the equatorial Pacific ocean to atmospheric forcing, *J. Phys. Oceanogr.*, 5, 572-584.

Figure captions:

Fig. 1: Meridional structures of (a) zonal current and (b) sea-level for Kelvin (solid line) and first Rossby (dotted line) modes calculated for a 2.5m/s phase speed. Each wave contribution at a given latitude can be obtained by multiplying the meridional structure by the corresponding coefficient, yielding cm/s for zonal current and 0.01 Pa for zonal wind stress, cm for sea-level (or dynamic height) anomaly.

Fig. 2: (a: top) standard deviation map of Arpege zonal wind stress over the 1985-1994 period (units are in Pa, contours are every 0.002Pa); (b: middle,) correlation map between Arpege zonal wind stress and zonal wind stress field reconstructed from only Kelvin and first Rossby oceanic wave forcing; (c: bottom) same as b, but explained variance map.

Fig. 3: Same as Figure 2 but considering dynamic height field. Units of dynamic height standard deviation are in cm.

Fig. 4: (a) Standard deviation of Kelvin wave coefficient from 130°E to 80°W: total signal (solid line), seasonal cycle (dotted line) and interannual anomalies (dashed line). Values are adimensionalised; (b) same as (a) but for first Rossby wave coefficient.

Fig. 5: Longitude time-plots of (a: left) Kelvin and (b: right) first Rossby wave coefficients. Values are adimensionalised. Amplitudes in sea-level and zonal geostrophic current anomalies can be calculated from corresponding wave structures displayed on figures 1 a and b.

Fig. 6: longitude time-plots of (a: left) Kelvin and (b: right) first Rossby wave coefficient seasonal cycles. The year is repeated 3 times.

Fig. 7: Same as in Figure 6, but for wave forcing coefficients.

Fig. 8: Interannual anomalies of Kelvin coefficients calculated from (a: left) OPA simulated dynamic height anomalies and (b: left) integration of Kelvin wave forcing along the wave characteristic.

Fig. 9: Same as in Figure 8, but for first Rossby.

Fig. 10: (a) Kelvin wave coefficients calculated from OPA simulated dynamic height anomalies relative to the Nov.86-Ott.88 period; (b) same as (a) but for first Rossby wave; (c) same as (a) but from GEOSAT sea-level data; (d) same as (b) but from GEOSAT sea-level data.

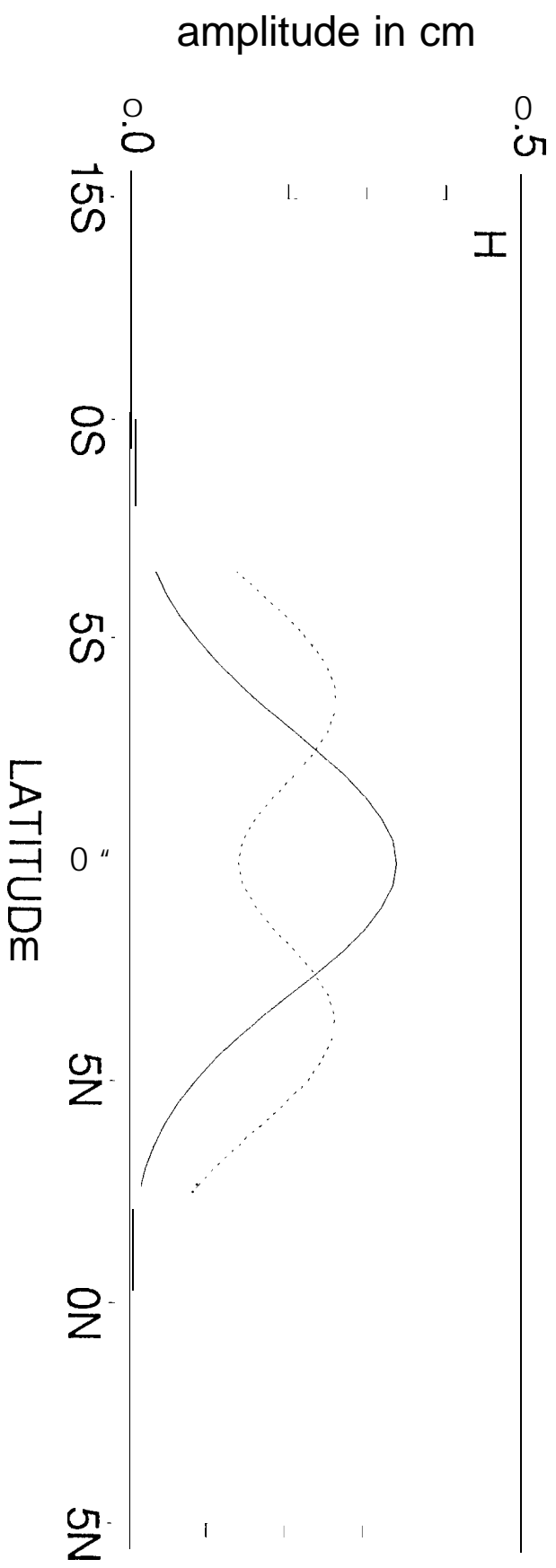
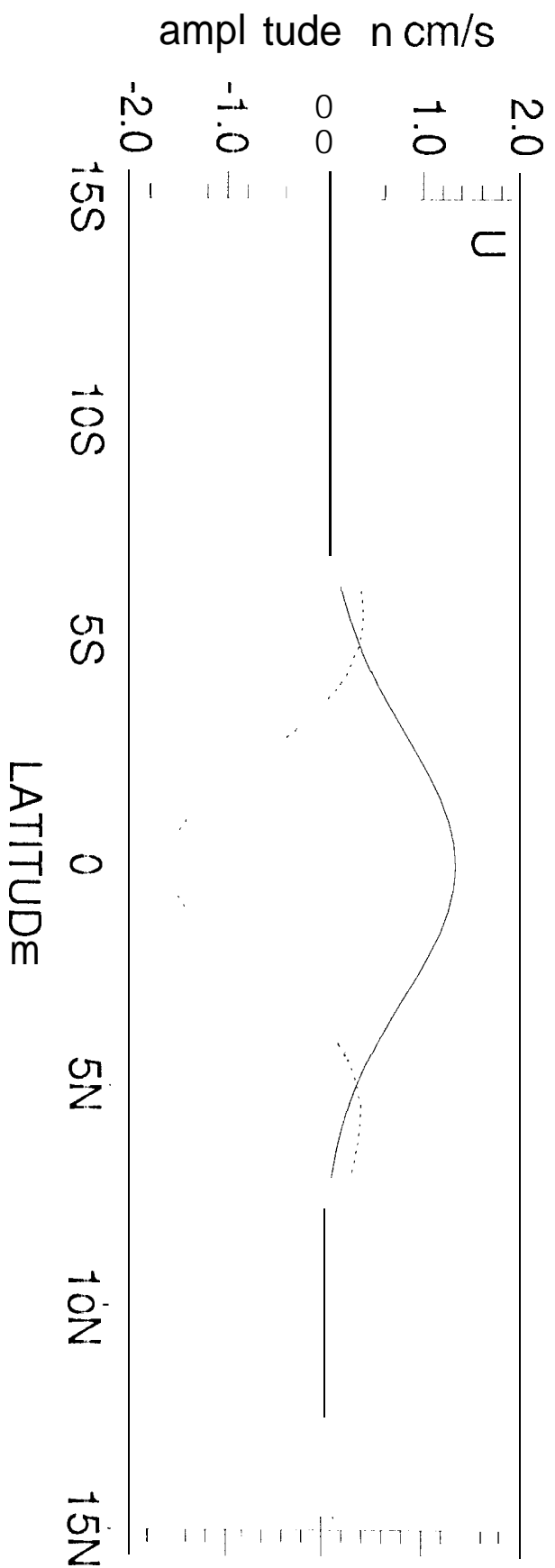
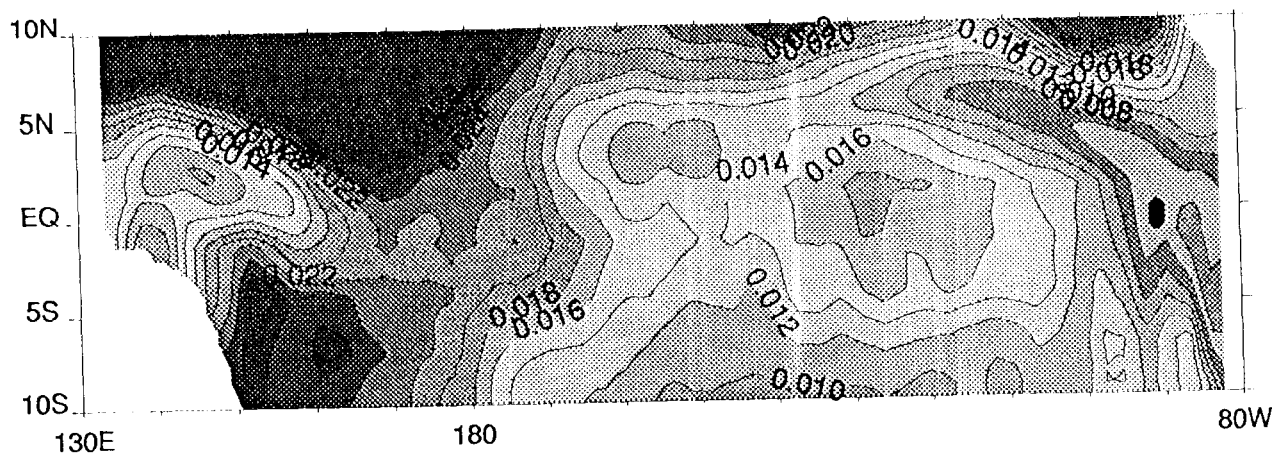


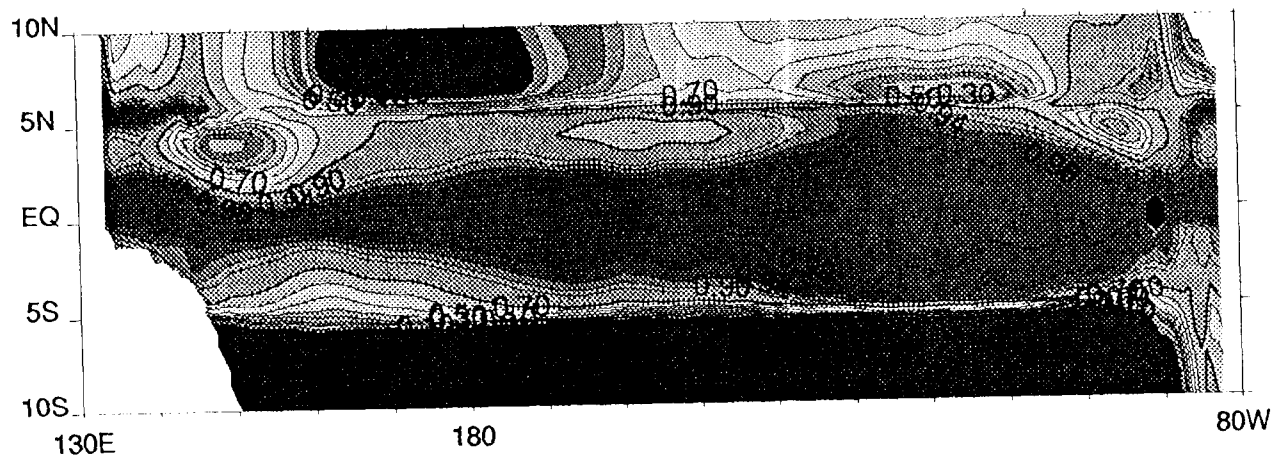
Fig. 1

Fig. 2

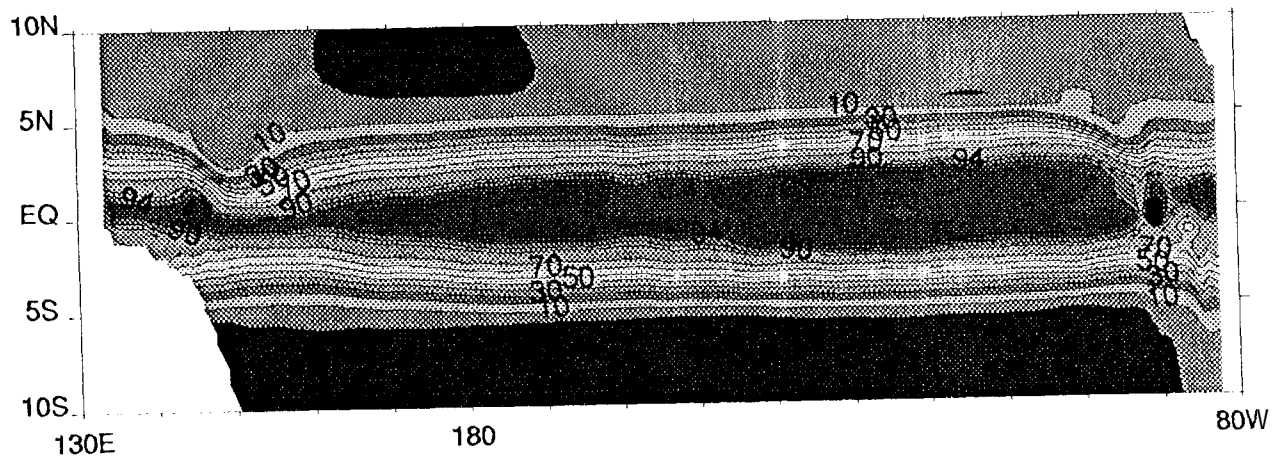
STD TX



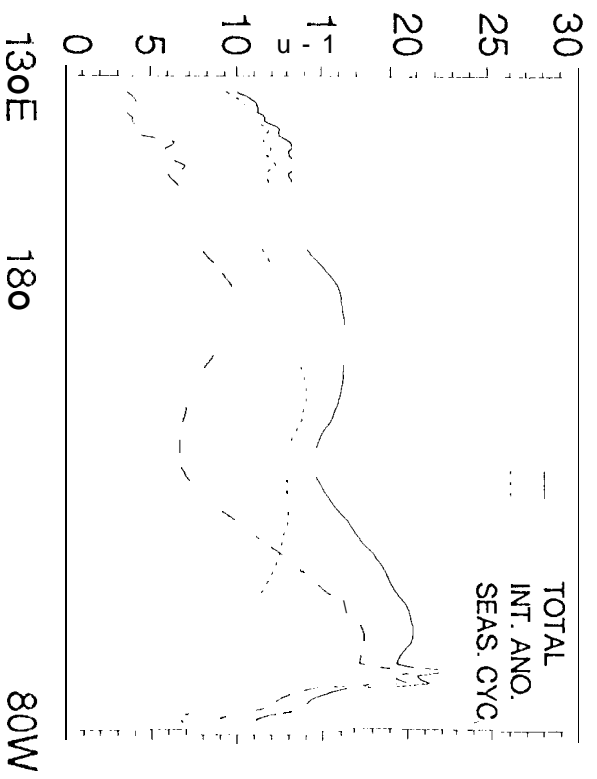
CORRELATION



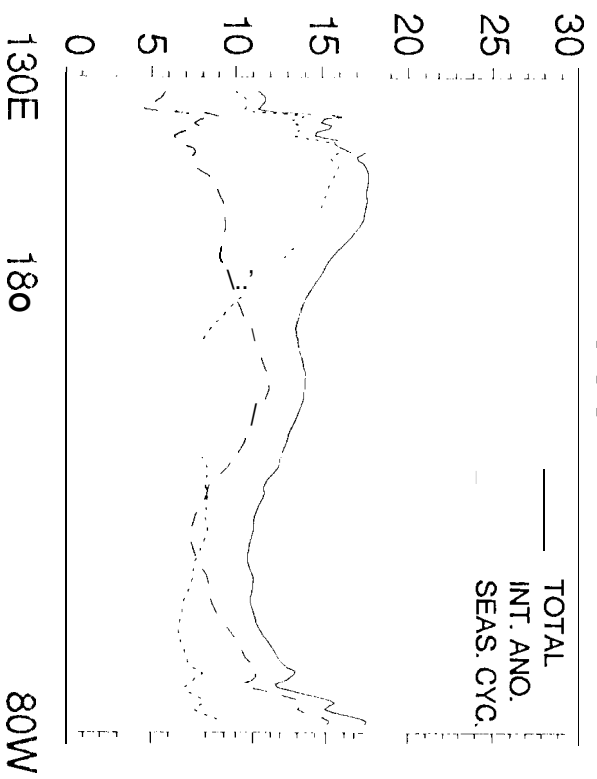
EXPLAINED VARIANCE (%)



KELVIN



ROSSBY1



Fig

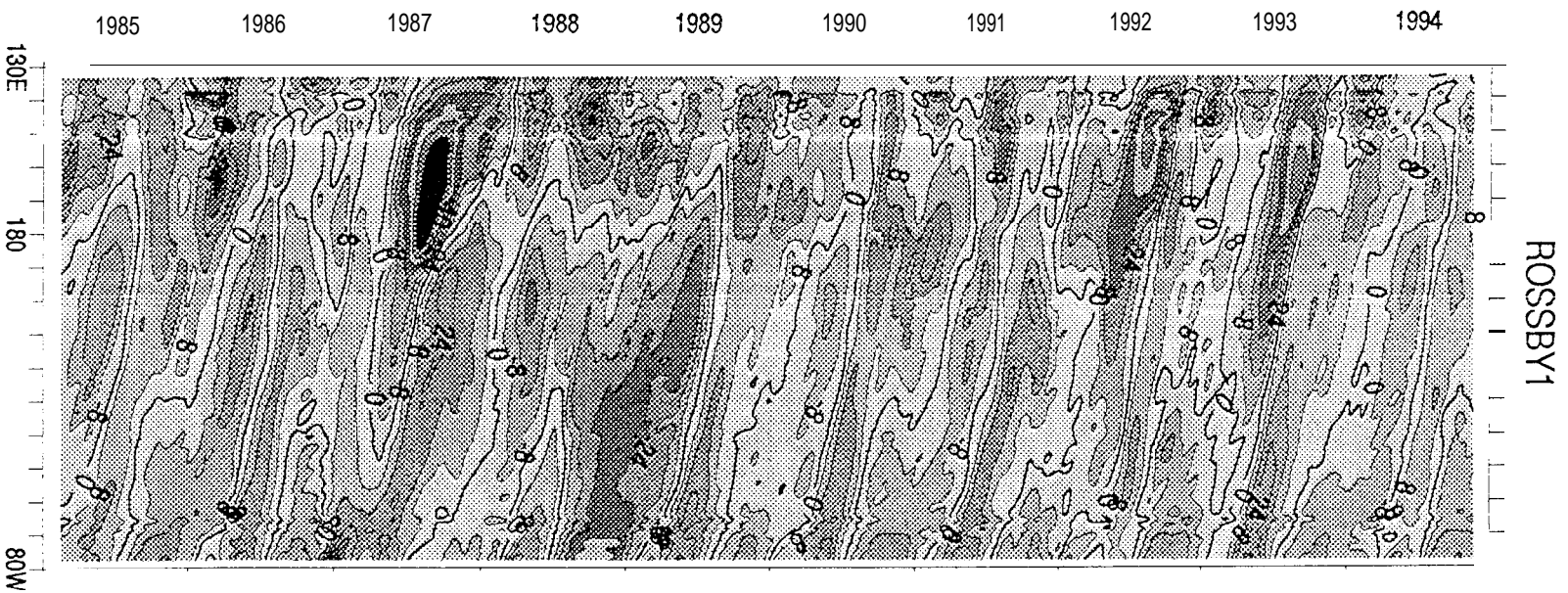
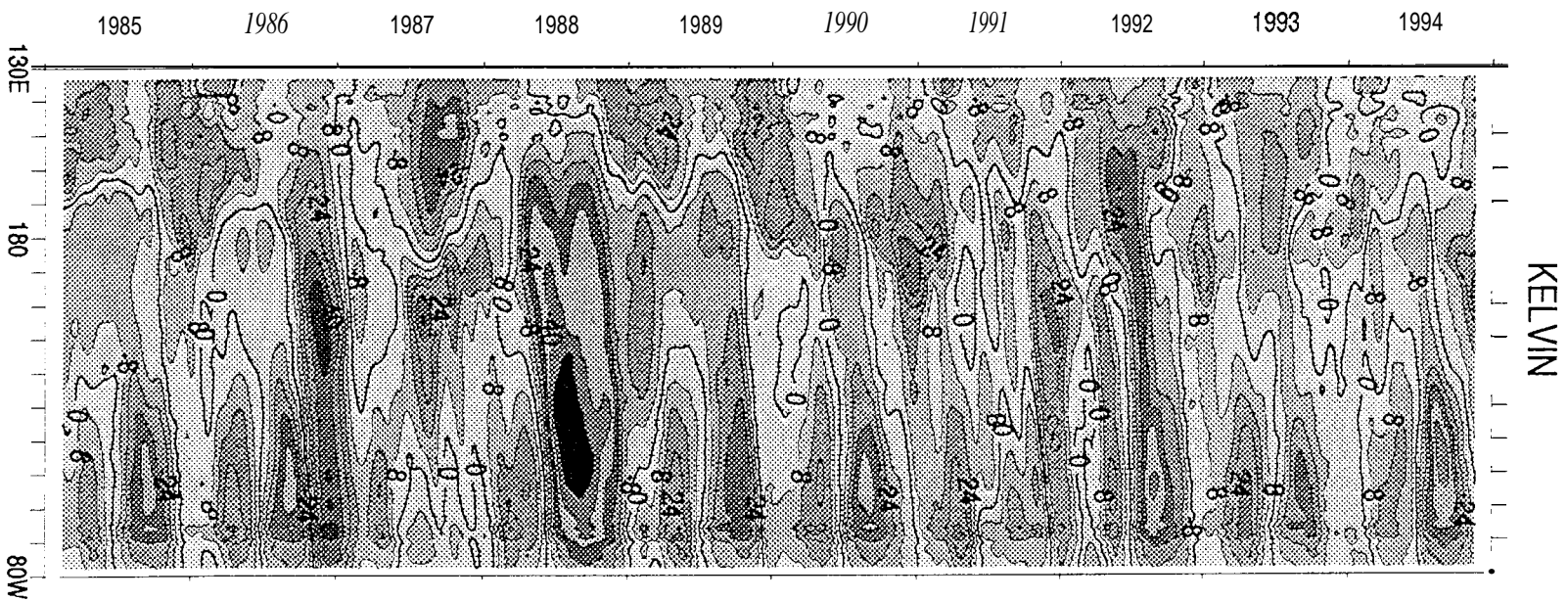


Fig. 5

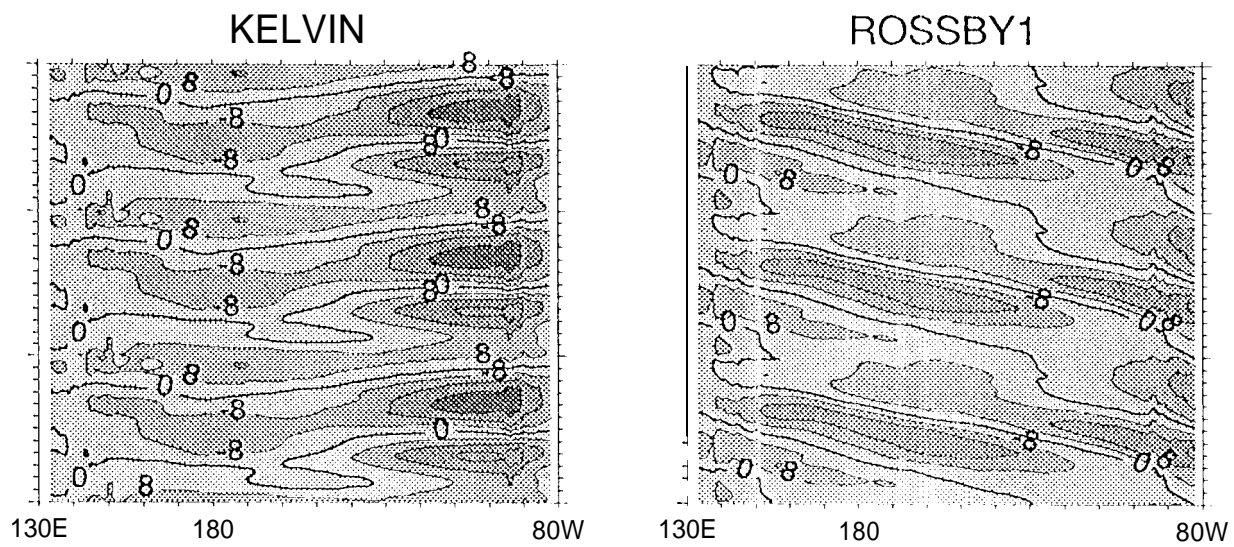


Fig. 6

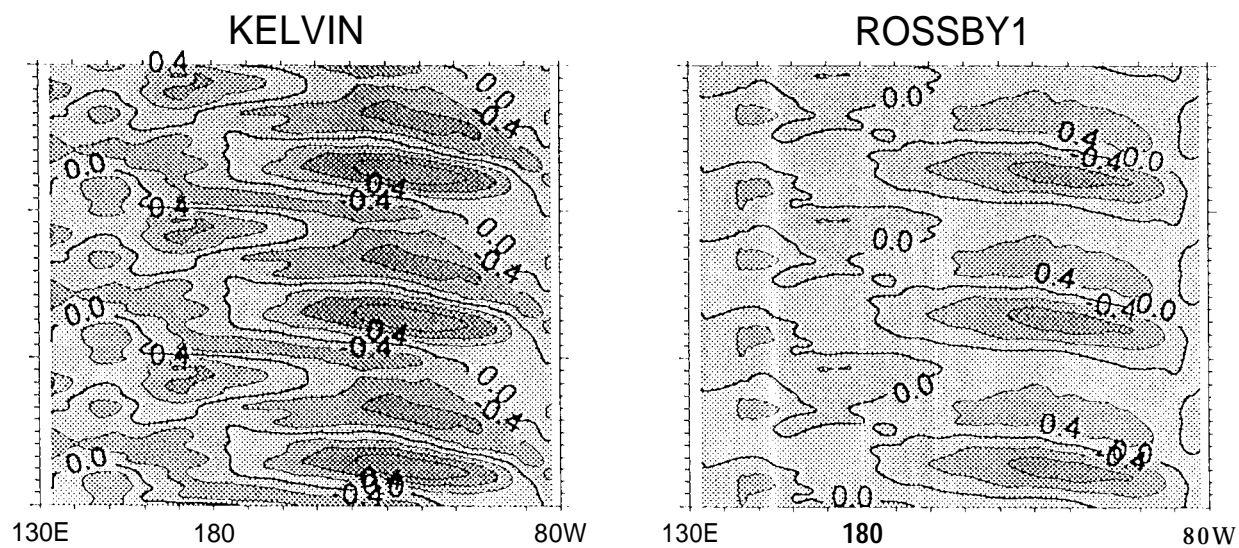
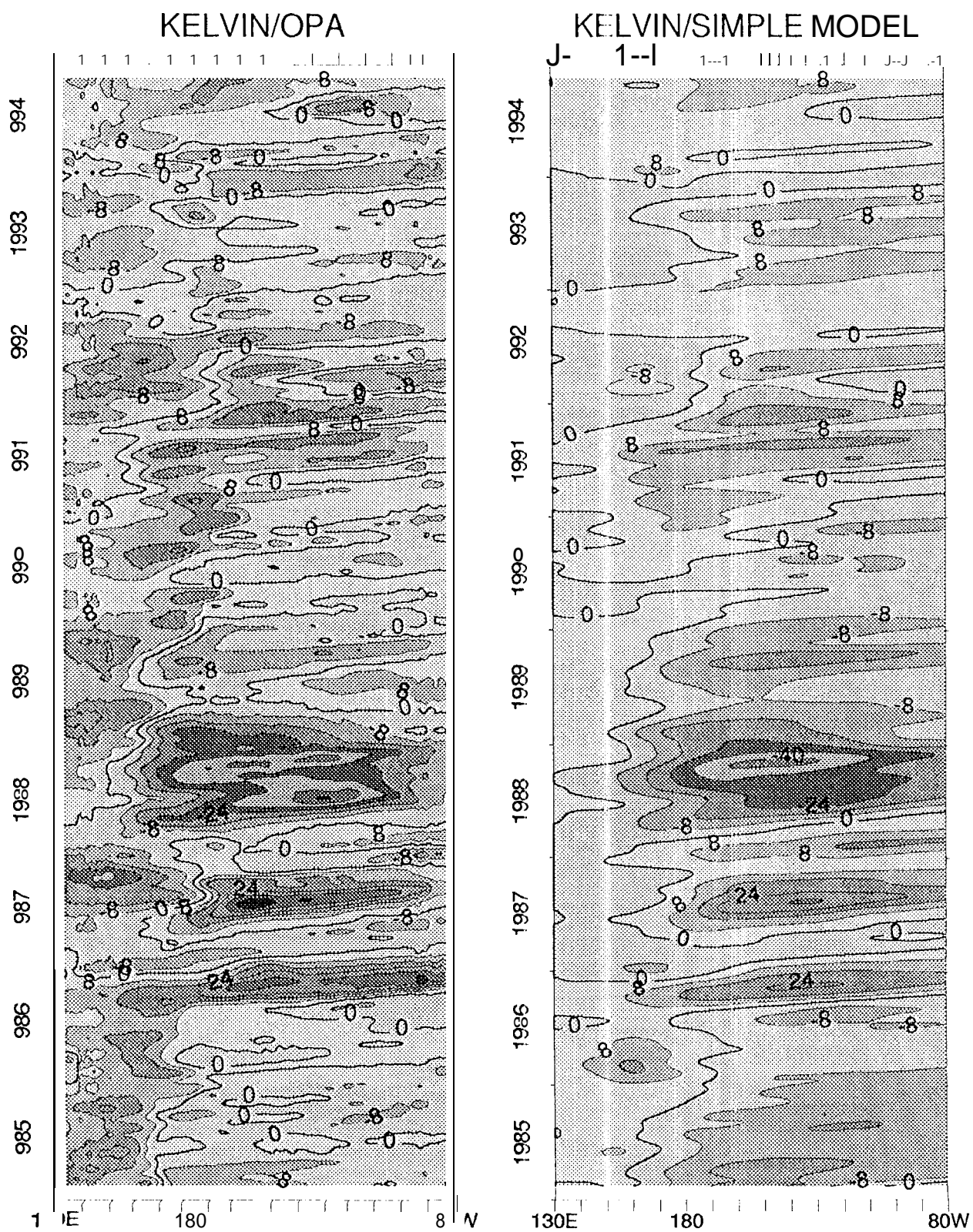


Fig. 7

Fig. 8



ROSSBY1/OPA

Fig 2

ROSSBY1/S M2LE MODEL

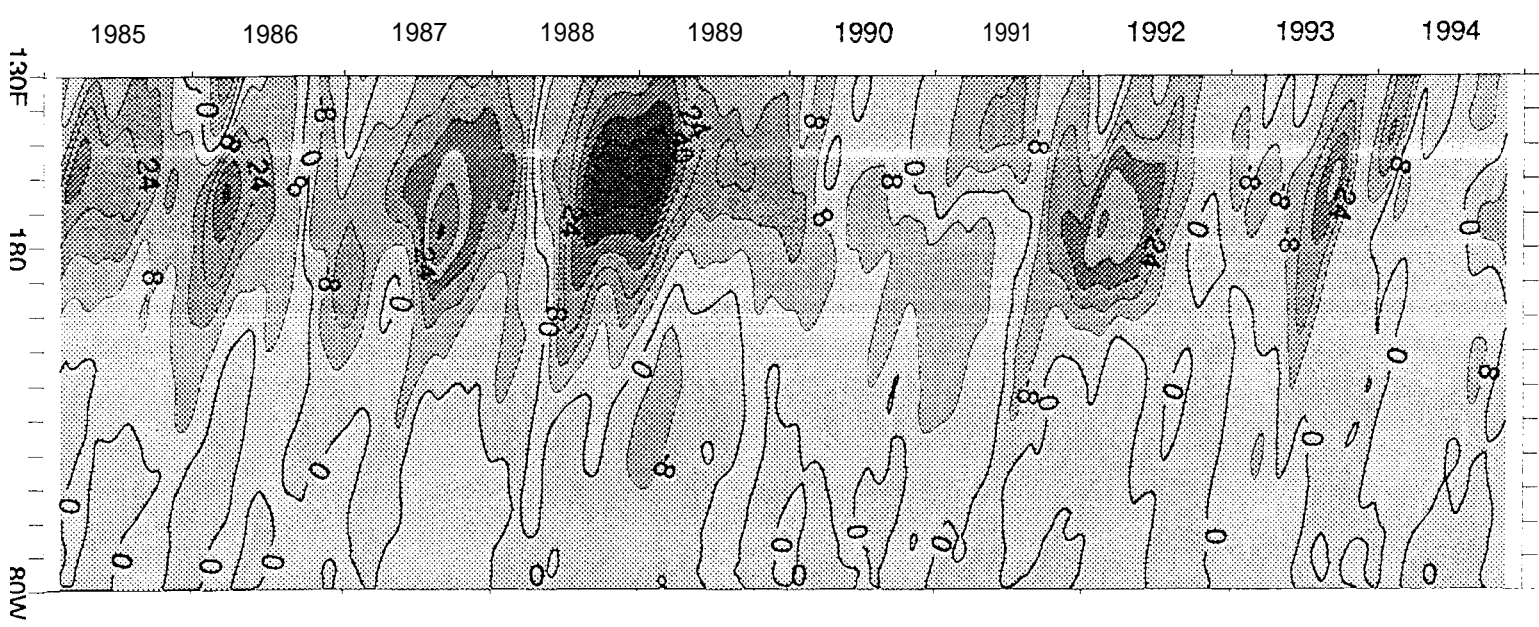
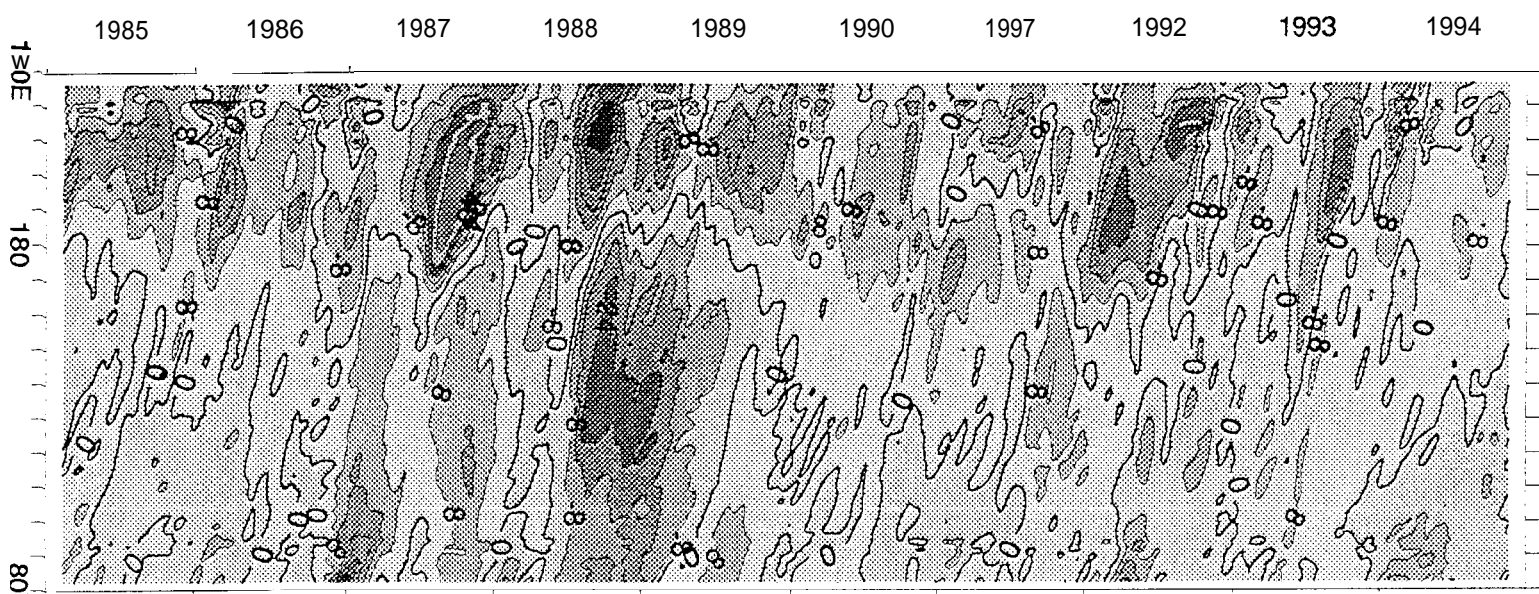
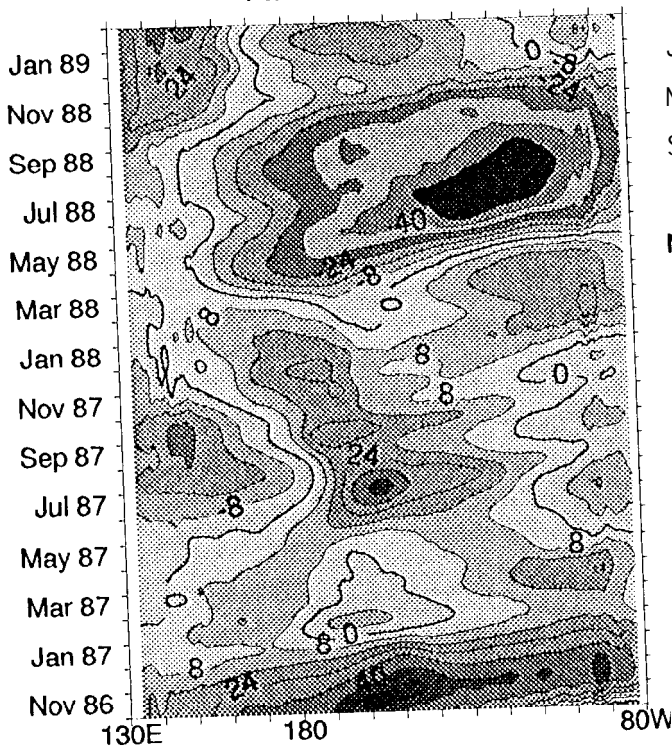
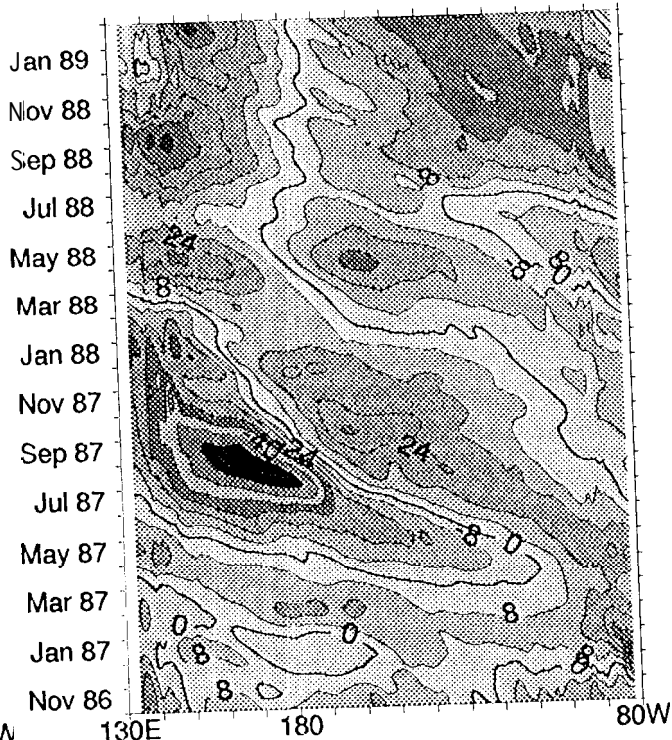


Fig 10 a-d

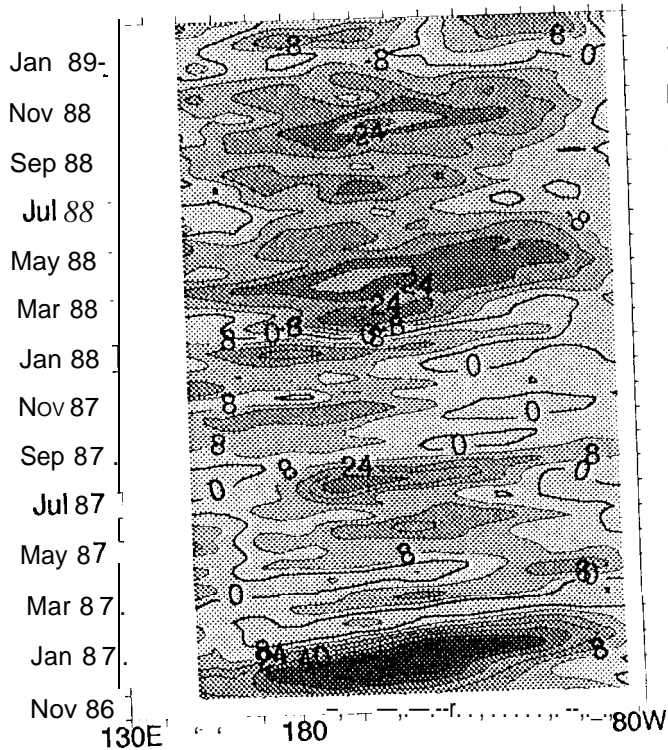
KELVIN/OPA



ROSSBY1/OPA



KELVIN/GEOSAT



ROSSBY1/GEOSAT

